



The $C(^3P) + NO(X^2\Pi) \rightarrow O(^3P) + CN(X^2\Sigma^+)$, $N(^2D)/N(^4S) + CO(X^1\Sigma^+)$ reaction: Rates, branching ratios, and final states from 15 K to 20 000 K

Cite as: J. Chem. Phys. **149**, 094305 (2018); <https://doi.org/10.1063/1.5046906>

Submitted: 03 July 2018 • Accepted: 27 August 2018 • Published Online: 07 September 2018

Debasish Koner,  Raymond J. Bemish and  Markus Meuwly



View Online



Export Citation



CrossMark

ARTICLES YOU MAY BE INTERESTED IN

Exhaustive state-to-state cross sections for reactive molecular collisions from importance sampling simulation and a neural network representation

The Journal of Chemical Physics **150**, 211101 (2019); <https://doi.org/10.1063/1.5097385>

N_3^+ : Full-dimensional ground state potential energy surface, vibrational energy levels, and dynamics

The Journal of Chemical Physics **153**, 044302 (2020); <https://doi.org/10.1063/5.0011957>

Non-conventional force fields for applications in spectroscopy and chemical reaction dynamics

The Journal of Chemical Physics **153**, 010901 (2020); <https://doi.org/10.1063/5.0009628>



Time to get excited.
Lock-in Amplifiers – from DC to 8.5 GHz

Find out more

Zurich Instruments

The $C(^3P) + NO(X^2\Pi) \rightarrow O(^3P) + CN(X^2\Sigma^+)$, $N(^2D)/N(^4S) + CO(X^1\Sigma^+)$ reaction: Rates, branching ratios, and final states from 15 K to 20 000 K

Debasish Koner,¹ Raymond J. Bemish,² and Markus Meuwly^{1,a)}

¹Department of Chemistry, University of Basel, Klingelbergstrasse 80, CH-4056 Basel, Switzerland

²Air Force Research Laboratory, Space Vehicles Directorate, Kirtland AFB, New Mexico 87117, USA

(Received 3 July 2018; accepted 27 August 2018; published online 7 September 2018)

The C + NO collision system is of interest in the area of high-temperature combustion and atmospheric chemistry. In this work, full dimensional potential energy surfaces for the $^2A'$, $^2A''$, and $^4A''$ electronic states of the [CNO] system have been constructed following a reproducing kernel Hilbert space approach. For this purpose, more than 50 000 *ab initio* energies are calculated at the MRCI+Q/aug-cc-pVTZ level of theory. The dynamical simulations for the $C(^3P) + NO(X^2\Pi) \rightarrow O(^3P) + CN(X^2\Sigma^+)$, $N(^2D)/N(^4S) + CO(X^1\Sigma^+)$ reactive collisions are carried out on the newly generated surfaces using the quasiclassical trajectory (QCT) calculation method to obtain reaction probabilities, rate coefficients, and the distribution of product states. Preliminary quantum calculations are also carried out on the surfaces to obtain the reaction probabilities and compared with QCT results. The effect of nonadiabatic transitions on the dynamics for this title reaction is explored within the Landau-Zener framework. QCT simulations have been performed to simulate molecular beam experiment for the title reaction at 0.06 and 0.23 eV of relative collision energies. Results obtained from theoretical calculations are in good agreement with the available experimental as well as theoretical data reported in the literature. Finally, the reaction is studied at temperatures that are not practically achievable in the laboratory environment to provide insight into the reaction dynamics at temperatures relevant to hypersonic flight. *Published by AIP Publishing.* <https://doi.org/10.1063/1.5046906>

I. INTRODUCTION

Carbon, nitrogen, and oxygen are among the dominant elements in the planetary atmosphere and in the interstellar medium. Studies involving the collisions between C-, N-, and O-containing species are potentially important in the area of low temperature reactions in the interstellar medium and high temperature combustion chemistry. The triatomic [CNO] system shows rich chemistry as varieties of reactive collisions are possible; see Fig. 1. Among those, the $C + NO \rightarrow O + CN$, $N + CO$ reactions play important roles in NO reburning and therefore removing the pollutant NO from the atmosphere.¹ The $C + NO \rightarrow O + CN$ reaction has immense importance in chemical phenomena in dense interstellar clouds, as the CN molecule—a spectroscopic probe and a precursor to many more complex molecules—is formed via this reaction.² As can be seen in Fig. 1, reactive collisions between $C(^3P) + NO(X^2\Pi)$ yield $O(^3P) + CN(X^2\Sigma^+)$ and $N(^2D) + CO(X^1\Sigma^+)$ adiabatically on the 2A surface, while nitrogen can be formed in its ground electronic state (4S) on the 4A surface. Being exothermic in nature and barrierless in the entrance channel, the title reaction can occur at low temperatures (<50 K) and is relevant to astrochemistry.

The investigation of the [CNO] system started in the late sixties, when the room temperature rates for $C(^3P)/$

$C(^1D) + NO \rightarrow O + CN$ were measured using vacuum ultraviolet flash photolysis.³ In 1971, the kinetics of $C(^3P)$ in the presence of nitric oxide was studied in the gas phase at room temperature which yielded a rate of $7.3 \pm 2.2 \times 10^{-11} \text{ cm}^3 \text{ molecule}^{-1} \text{ s}^{-1}$.⁴ Later in a similar study but using the signal averaging analysis of the raw data, the rate was found to be $4.8 \pm 0.8 \times 10^{-11} \text{ cm}^3 \text{ molecule}^{-1} \text{ s}^{-1}$.⁵ Next, the $O(^3P) + CN$ reaction was investigated using flash photolysis in a discharge flow reactor and two different electronic states 4S and 2D of the nitrogen atom in a ratio of 20% and 80% at room temperature were found.⁶ These results were also supported by quasiclassical trajectory (QCT) calculations on an empirical London-Eyring-Polanyi-Sato (LEPS) type surface.⁶ These findings suggest that both 2A and 4A electronic states of [CNO] participate in the dynamics at room temperature. A subsequent theoretical study suggested that the $C + NO \rightarrow O + CN$ reaction occurs significantly only on the 2A electronic states of [CNO].⁷

Then, the rates and branching fractions for the $C + NO$ reaction were determined via shock tube experiment over a wide temperature range (1550–4050 K).⁸ The branching ratio of the CO product was found to be constant at 0.6 over the temperature range 2400–4000 K, which agrees with experiments at room temperature in a low pressure fast flow reactor which also yielded a branching of 0.6 with a rate $5.4 \pm 0.8 \times 10^{-11} \text{ cm}^3 \text{ molecule}^{-1} \text{ s}^{-1}$.⁹ Finally, the overall rate constant for the $C + NO$ reaction from room temperature to very low temperatures (15 K) was measured.¹⁰ It was found that the

^{a)}m.meuwly@unibas.ch

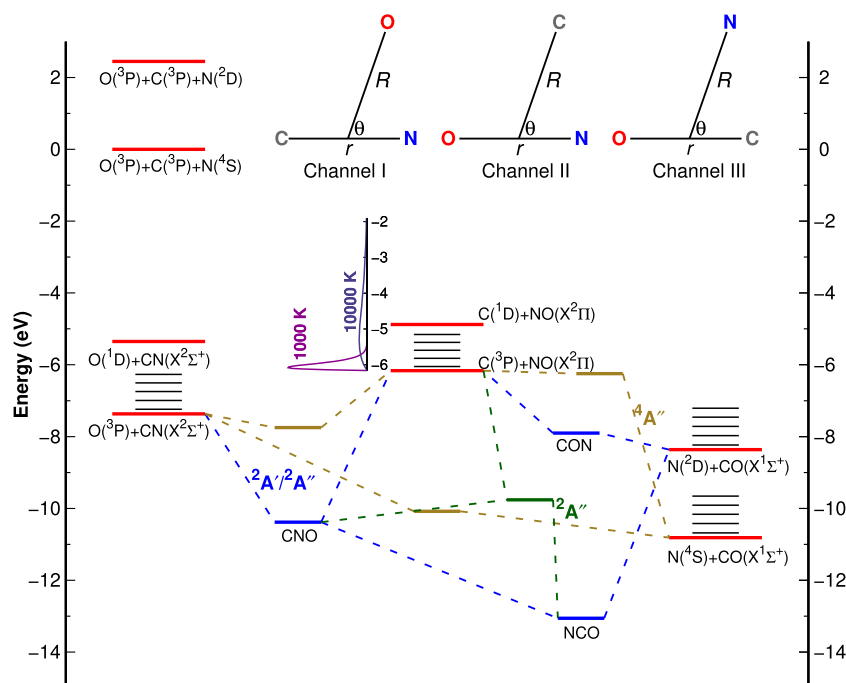


FIG. 1. Schematic energy profile for the [CNO] system. Different channels and minima are also shown. The blue lines connect the configurations of ${}^2A'$ and ${}^2A''$ states. The minimum, shown as a dark green line, exists only for the ${}^2A''$ PES, and it is nonlinear. The olive lines connect the nonlinear minima of ${}^4A''$ state configurations. Three different grids as defined for the three different channels for the *ab initio* energies are shown at top right. The Maxwell-Boltzmann distribution of the thermal energies in channel II is shown at 1000 K and 10 000 K. The first five vibrational states ($v = 0$ to 4, $j = 0$) are shown in the three asymptotic geometries as black lines.

rate increases with decreasing temperature, as expected for a barrierless reaction.

Crossed molecular beam experiments were performed for this reaction at 0.06 and 0.23 eV of relative translational energies, and the ro-vibrational distributions of the CN product were measured using laser-induced fluorescence.¹¹ In a subsequent study, the reactive cross sections for the reaction at relative translational energies 0.038 to 0.163 eV were measured.¹² Several theoretical investigations have been carried out later on the 2A surface to investigate the ro-vibrational distribution of CN at both the collision energies.^{13–17} The ro-vibrational distribution of CN was best described when the ${}^4A''$ electronic state was adiabatically included in the dynamical simulations.¹⁷

The ${}^2A'$, ${}^2A''$, and ${}^4A''$ symmetries have been found to be the lowest-lying states for the [CNO] system for nonlinear configurations.^{18,19} A LEPS-type potential energy surface (PES) for the ${}^2A'$ symmetry of the [CNO] system has been constructed¹³ followed by a many body expansion fit of the ${}^2A''$ surface from complete active space perturbation theory second order (CASPT2) energies.¹⁵ This was further improved by including more *ab initio* energies for nonlinear geometries and analytically describing the long-range part.²⁰ In the subsequent work, the PESs for the ${}^2A'$ and ${}^4A''$ symmetries of [CNO] using CASPT2 calculations and the same parameterization of the PES were constructed.^{16,17} The C + NO reaction was investigated by means of QCT calculations in a series of studies.^{16,17,20,21} There the focus was on calculating the rate coefficients over a temperature range starting from low (<10 K) to 5000 K. The results for the C + NO reaction agree well with the experimental results when the dynamics were carried out on the ${}^4A''$ surface along with ${}^2A'$ and ${}^2A''$ PESs.¹⁷ However, the branching fraction of the CO product underestimates the experimental findings and including nonadiabatic transitions between different electronic states in the

dynamics was suggested to improve the theoretical results. In a recent study, adiabatic capture centrifugal sudden approximation was used as an alternative method of QCT to study the C + NO reaction.²² Very recently, a double many-body expansion (DMBE) surface is generated for the ${}^2A'$ electronic state of [CNO] using MRCI-F12/cc-pVQZ-F12 energies²³ which has to date not been used in a dynamics simulation.

The [CNO] system exhibits the Renner-Teller effect. For linear geometries, the ${}^2A'$ and ${}^2A''$ PESs become degenerate and correspond to a ${}^2\Pi$ symmetry. However, for bent geometries, the ${}^2\Pi$ symmetry splits into ${}^2A'$ and ${}^2A''$ states. Thus for excited vibrational states, there is a possibility of nonadiabatic transitions between the ${}^2A'$ and ${}^2A''$ states. There are crossings between the doublet and quartet PESs in the N + CO product channel, and these states are coupled via spin-orbit interactions which can lead to transitions between them. Thus the inclusion of the nonadiabatic effect in the dynamics of the C + NO reaction may provide additional insights into the branching ratio of the products and the reaction paths. As the C + NO reaction is also important in combustion chemistry and NO plays a crucial role in the chemistry near the surface of a space vehicle during atmospheric re-entry,²⁴ studying the dynamics for this reaction at temperature relevant to the hypersonic flight regime will help to build a computational model of these situations. At this stage, the particular interest is (a) to determine accurate PESs for the ${}^2A'$, ${}^2A''$, and ${}^4A''$ symmetries for [CNO] based on high level *ab initio* calculations; (b) to use a robust method, the reproducing kernel Hilbert space (RKHS) for the interpolation of the PES; and (c) to study the dynamics for a range of temperatures with a particular focus on conditions relevant to the hypersonic flight regime by including and excluding nonadiabatic effects in the dynamics.

In the present work, global PESs have been constructed for the ${}^2A'$, ${}^2A''$, and ${}^4A''$ symmetries for the [CNO] system

from a large number (>50 000) of MRCI+Q/aug-cc-pVTZ energies using the reproducing kernel Hilbert space (RKHS) technique. All possible product channels are described with the correct asymptotic behavior (R^{-6}) for neutral-neutral interactions. The reaction dynamics for the C + NO reaction are characterized using quasiclassical trajectory simulations which are validated vis-a-vis time independent quantum mechanical (TIQM) scattering calculations. Rate coefficients for the title reaction are calculated over a wide range of temperatures, ranging from 15 K to 5000 K using both adiabatic and nonadiabatic QCT simulations. Distributions of product states are calculated for the C + NO reaction at 0.06 and 0.23 eV of collision energies using the QCT method. These allow the validation of the QCT simulations by direct comparison with experiments.⁸⁻¹¹ From the validated simulations, we further investigate the dynamics under conditions corresponding to high-temperature (5000–20 000 K) hypersonic flow by determining corresponding thermal rates, distributions of products, and vibrational relaxation as experiments under these extreme conditions are difficult or even impossible.

This article is organized as follows. In Sec. II, the computational methodologies for computing the PESs and carrying out the dynamics simulations are outlined. The results are presented and discussed in Sec. III, and conclusions are presented in Sec. IV.

II. COMPUTATIONAL METHODS

A. The potential energy surfaces

All electronic structure calculations were performed using the Molpro software.²⁵ The multireference configuration interaction level of theory including the Davidson correction (MRCI+Q) with the augmented Dunning type correlation consistent polarized triple zeta (aug-cc-pVTZ) basis set²⁶⁻²⁸ was chosen to compute all *ab initio* energies. Initial orbitals for the MRCI calculations were computed using the complete active space self-consistent field (CASSCF) method, where the 1s orbitals of all the atoms were treated as core orbitals. In order to be consistent with the active orbitals, for all the *ab initio* calculations, the C_s symmetry was used.

For both 2A electronic states, three reactive channels are possible: (I) $O(^3P) + CN(X^2\Sigma^+)$, (II) $C(^3P) + NO(X^2\Pi)$, and (III) $N(^2D) + CO(X^1\Sigma^+)$, while for the $^4A''$ electronic state, channel (III) corresponds to $N(^4S) + CO(X^1\Sigma^+)$. For the electronic structure calculations, three-dimensional grids in Jacobi coordinates (R, r, θ) are used for each of the channels (see Fig. 1). Here, r is the diatomic bond length, R is the distance from the center of mass of the diatom to the free atom, and θ is the angle between \vec{r} and \vec{R} . For all PESs, 13 Gauss-Legendre quadrature points define the angular grid between 0° and 180° . Details of the radial grids for all channels and for both electronic states are tabulated in Table I.

The reproducing kernel Hilbert space (RKHS) technique²⁹ is used to represent the discrete points from the electronic structure calculations. According to the RKHS theorem, the approximated value $\tilde{f}(\mathbf{x})$ of a function $f(\mathbf{x})$ can be obtained

TABLE I. Numerical grids for the radial coordinates for the *ab initio* energy calculations (lengths are given in a_0).

	Channel I			Channel II			Channel III		
	$^2A'$	$^2A''$	$^4A''$	$^2A'$	$^2A''$	$^4A''$	$^2A'$	$^2A''$	$^4A''$
N_r	19	19	19	19	19	19	19	19	19
r_{\min}	1.45	1.45	1.45	1.5	1.5	1.5	1.5	1.5	1.5
r_{\max}	4.0	4.0	4.0	4.0	4.0	4.0	4.0	4.0	4.0
N_R	23	22	24	21	23	24	21	23	24
R_{\min}	1.4	1.65	1.65	1.4	1.65	1.65	1.4	1.65	1.65
R_{\max}	12.0	12.0	12.0	12.0	12.0	12.0	12.0	12.0	12.0

from a set of known values $f(\mathbf{x}_i)$ as a linear combination of kernel polynomials

$$\tilde{f}(\mathbf{x}) = \sum_{i=1}^N c_i K(\mathbf{x}, \mathbf{x}_i), \quad (1)$$

where c_i are the coefficients and $K(\mathbf{x}, \mathbf{x}_i)$ is the reproducing kernel. The coefficients are determined from the values $f(\mathbf{x}_i)$ by solving a set of linear equations

$$f(\mathbf{x}_j) = \sum_{i=1}^N c_i K(\mathbf{x}_i, \mathbf{x}_j). \quad (2)$$

A reproducing kernel exactly reproduces the values of the function at the known points. For a multidimensional function, the D -dimensional kernel is the product of D 1-dimensional kernels $k(x, x')$,

$$K(\mathbf{x}, \mathbf{x}') = \prod_{d=1}^D k^{(d)}(x^{(d)}, x'^{(d)}), \quad (3)$$

where $k^{(d)}(x^{(d)}, x'^{(d)})$ are the 1-dimensional kernels for each of the d dimensions.

For both radial dimensions (r and R), a reciprocal power decay kernel

$$k^{2,6}(x, x') = \frac{1}{14} \frac{1}{x_{>}^7} - \frac{1}{18} \frac{x_{<}}{x_{>}^8}, \quad (4)$$

was used, where $x_{>}$ and $x_{<}$ are the larger and smaller values of x and x' , respectively. This kernel smoothly decays to zero $\propto \frac{1}{x^6}$ which gives the correct long-range behavior for neutral atom-diatom type interactions. For the angular degree of freedom, a Taylor spline kernel is used,

$$k^2(z, z') = 1 + z_{<}z_{>} + 2z_{<}^2z_{>} - \frac{2}{3}z_{<}^3, \quad (5)$$

where $z_{>}$ and $z_{<}$ are similar to $x_{>}$ and $x_{<}$ and

$$z = \frac{1 - \cos \theta}{2}, \quad (6)$$

with $z \in [0, 1]$. Finally, the 3-dimensional kernel is

$$K(\mathbf{x}, \mathbf{x}') = k^{2,6}(R, R')k^{2,6}(r, r')k^2(z, z'). \quad (7)$$

A computationally efficient toolkit is used to calculate the coefficients and evaluate the function.³⁰

As the kernels decay to zero asymptotically, it is necessary to subtract the value of the diatomic potential energy,

$V(R \rightarrow \infty, r)$, from the *ab initio* energies $V(R, r, \theta)$ for each value of r and then interpolate the new data set ($V'(R, r, \theta) = V(R, r, \theta) - V(R \rightarrow \infty, r)$) with an RKHS. For this purpose, the diatomic potentials are calculated separately and interpolated within the RKHS framework. Thus, the energy of a particular point (R_0, r_0, θ_0) is

$$V(R_0, r_0, \theta_0) = V'(R_0, r_0, \theta_0) + V(R \rightarrow \infty, r_0). \quad (8)$$

The same procedure was previously followed for NO_2 , ArN_2^+ , N_2O , and ArCO .^{31–34} Finally, the global PES for an electronic state is constructed by smoothly connecting the three PESs for channels I to III using a switching function ($w_i(r)$) according to

$$V(\mathbf{r}) = \sum_{j=1}^3 w_j(r_j) V_j(\mathbf{r}), \quad (9)$$

where \mathbf{r} are the three internuclear distances. The switching function is

$$w_i(r) = \frac{e^{-(r_i/dr)^2}}{\sum_{j=1}^3 e^{-(r_j/dr_j)^2}}, \quad (10)$$

where dr_j are the different constants for channels I, II, and III and for different states (0.71, 0.69, 0.68 a_0 for the $^2A'$ state, 0.48, 0.40, 0.28 a_0 for the $^2A''$ state, and 1.06, 0.80, 1.0 a_0 for the $^4A''$ state). These values were optimized by the least square fitting method.

As the nitrogen atom is in a 2D state for channel III (2A), the energy $\Delta E = E_{\text{N}(^2D)} - E_{\text{N}(^4S)} = 2.4497$ eV is added to the interpolant to obtain the correct asymptotic behavior in the region where all atoms are well separated.

B. Quasiclassical trajectory calculation method

The QCT method followed in this work has been extensively described in Refs. 35 and 36. Hamilton's coupled differential equations of motion are solved using the fourth-order Runge-Kutta numerical method. Initial conditions for a trajectory are sampled using a standard Monte Carlo sampling method.³⁵ The reactant and product ro-vibrational states are determined using the semiclassical theory of bound states.

Since the ro-vibrational states of the product diatom are continuous numbers, these states are assigned by rounding the real numbers to suitable integer values. Two schemes for that are histogram binning (HB), rounding values to the nearest integers, and Gaussian binning, weighing each trajectory with a Gaussian shaped function centered on integer values.^{37,38} In this work, both schemes were tested and yielded similar results. For consistency, we only report the HB results. The time step was $\Delta t = 0.05$ fs which guaranteed the conservation of the total energy and angular momentum with an average error at the sixth and eighth decimal places, respectively.

The reaction probability at a fixed collision energy (E_c) for a particular total angular momentum (J) is

$$P_{v,j \rightarrow v',j'}(J, E_c) = \frac{N_{v',j'}}{N_{\text{tot}}}, \quad (11)$$

with an associated statistical sampling error

$$\Delta P_{v,j \rightarrow v',j'}(J, E_c) = \frac{N_{v',j'}}{N_{\text{tot}}} \sqrt{\frac{N_{\text{tot}} - N_{v',j'}}{N_{v',j'} N_{\text{tot}}}}, \quad (12)$$

where $N_{v',j'}$ is the number of reactive trajectories corresponding to the final state (v', j') of interest and N_{tot} is the total number of trajectories.

The state selected cross section is then computed as

$$\sigma_{v,j \rightarrow v',j'}(E_c) = \pi b_{\text{max}}^2 \frac{N_{v',j'}}{N_{\text{tot}}}, \quad (13)$$

where b_{max} is the maximum impact parameter for which a reactive collision can occur. The rate coefficient at a particular temperature is obtained from

$$k(T) = g(T) \sqrt{\frac{8k_B T}{\pi \mu}} \pi b_{\text{max}}^2 \frac{N_{v',j'}}{N_{\text{tot}}}, \quad (14)$$

where $g(T)$ is the electronic degeneracy factor, k_B is the Boltzmann constant, and μ is the reduced mass of the collision system.

For the $\text{C}(^3P) + \text{NO}(X^2\Pi)$ reaction, the degeneracy factors are^{17,21}

$$g_{2A}^{\text{C+NO}}(T) = \frac{1 + \exp(-23.6/T)}{[1 + 3 \exp(-23.6/T) + 5 \exp(-62.4/T)][2 + 2 \exp(-172.4/T)]} \quad (15)$$

and

$$g_{4A}^{\text{C+NO}}(T) = \frac{4 \exp(-23.6/T)}{[1 + 3 \exp(-23.6/T) + 5 \exp(-62.4/T)][2 + 2 \exp(-172.4/T)]}, \quad (16)$$

for the 2A and 4A states, respectively. Here, the first three terms in the denominator express the electronic partition functions of $\text{C}(^3P)$ considering J -values 0, 1, and 2 and the last two terms represent the electronic partition functions of the NO molecule for two spin orbit states, 1/2 and 3/2. The terms

in the numerator are the electronic partition functions for the states of CNO, which connects the reactant channels and the symmetry considered. The constant parameters in each term are the degeneracy of that J state, while the exponential factor determines the population at temperature T . The energy

separation between 3P_0 and 3P_1 states and 3P_1 and 3P_2 states of the carbon atom is 23.6 K and 62.4 K, respectively, whereas for NO, the energy separation between $^2\Pi_{1/2}$ and $^2\Pi_{3/2}$ states is 172.4 K.

The initial relative translational energies (E_c) of the reactants are sampled from a Maxwell-Boltzmann distribution at temperature T ,

$$f(E_c) = \frac{E_c}{k_B T} \exp\left(-\frac{E_c}{k_B T}\right). \quad (17)$$

The ro-vibrational states of the diatoms at a particular temperature can be expressed as Boltzmann distribution

$$p_{v,j}(T) = \frac{(2j+1) \exp(-\frac{\varepsilon_{v,j}}{k_B T})}{Q_{\text{rovib}}}, \quad (18)$$

where $\varepsilon_{v,j}$ is the ro-vibrational energy and Q_{rovib} is the ro-vibrational partition function

$$Q_{\text{rovib}} = \sum_{v'=0}^{v_{\text{max}}} \sum_{j'=0}^{j_{\text{max}}(v')} (2j'+1) \exp\left(-\frac{\varepsilon_{v',j'}}{k_B T}\right). \quad (19)$$

Rate coefficients for the $C(^3P) + NO(X^2\Pi) \rightarrow O(^3P) + CN(X^2\Sigma^+)$, $N(^2D)/N(^4S) + CO(X^1\Sigma^+)$ reactions are calculated between 15 K and 20 000 K (15, 30, 50, 100, 200, 300, 500, 700, 1000, 2000, 3000, 4000, 5000, 7000, 10 000, 12 000, 15 000, 17 000, and 20 000 K) by running a total number of 40 000 trajectory calculations at each temperature on each surface.

Stratified sampling^{35,39} is used in this work to generate impact parameters b in the interval $0 \leq b \leq b_{\text{max}}$. In this approach, the interval between 0 and b_{max} is equally divided into K strata. Each stratum k is defined from a minimum value of $b = b_{k-1}$ to a maximum value of $b = b_k$, where $b_0 = 0$ and $b_K = b_{\text{max}}$. For a trajectory, an integer (k) between 1 and K is selected randomly, and then the impact parameter is sampled as $b_k \sqrt{\eta}$, where η is a random number between 0 and 1. The fractional volume or weight of the k th stratum in “ b -space” is³⁹

$$V_k = \frac{b_k^2 - b_{k-1}^2}{b_{\text{max}}^2}, \quad (20)$$

where

$$\sum_{k=1}^K V_k = 1.$$

Thus, the reaction probability averaged over all strata is

$$\langle P \rangle = \sum_{k=1}^K V_k \frac{N_k^r}{N_k}, \quad (21)$$

where N_k^r and N_k are the number of reactive trajectories and total number of trajectories in the k th stratum, respectively. In Table II, the maximum impact parameters and initial

TABLE II. Details of maximum impact parameters (b_{max}), initial separations (ρ_0), maximum of R_{NO} ($R_{\text{NO}}^{\text{max}}$), and maximum of R_{CN} ($R_{\text{CN}}^{\text{max}}$) used in the QCT simulations. The units of distances are in a_0 .

T (K)	b_{max}	ρ_0	$R_{\text{NO}}^{\text{max}}$	$R_{\text{CN}}^{\text{max}}$
15–30	28.0	35.0	25.0	40.0
50–200	26.0	32.0	25.0	37.0
300–700	24.0	30.0	25.0	35.0
1 000–5 000	18.0	24.0	25.0	30.0
7 000–20 000	12.0	18.0	25.0	25.0

separation between the reactant species are given. For a trajectory, the integration was stopped when either R_{NO} or R_{CN} was large enough (see Table II for the values).

The trajectory surface hopping (TSH) method⁴⁰ is also used in this work to determine thermal rates including nonadiabatic transitions within the Landau-Zener^{41,42} formalism. In this work, a modified version of the Landau-Zener expression as derived by Belyaev and Lebedev^{43,44} is used. The same formula was followed by Domcke and co-workers to study different nonadiabatic systems using the TSH method.^{45,46} The modified formula depends only on the adiabatic potential energies of the states involved in the transition at time t_c ,

$$P_{\text{LZ}}^{j \rightarrow k} = \exp\left(-\frac{\pi}{2\hbar} \sqrt{\frac{\Delta V_{jk}^a(R(t_c))^3}{\frac{d^2}{dt^2} \Delta V_{jk}^a(R(t_c))}}\right). \quad (22)$$

Here, $P_{\text{LZ}}^{j \rightarrow k}$ is the transition probability from state j to state k and $\Delta V_{jk}^a(R)$ is the adiabatic energy difference between these states. The trajectories are started from a selected initial electronic state, and if there is crossing between the present electronic state j and a different electronic state k , $P_{\text{LZ}}^{j \rightarrow k}$ is calculated and compared with a random number $\xi \in [0, 1]$. If $P_{\text{LZ}}^{j \rightarrow k} \geq \xi$, the trajectory hops from state j to state k . In order to ensure conservation of total energy and total angular momentum, momentum corrections along different degrees of freedom have been employed,⁴⁷

$$\mathbf{p}' = \mathbf{p} - \hat{\mathbf{n}} \frac{\hat{\mathbf{n}} \mathbf{M}^{-1} \mathbf{p}}{\hat{\mathbf{n}} \mathbf{M}^{-1} \hat{\mathbf{n}}} \left[1 - \left(1 - 2\Delta E \frac{\hat{\mathbf{n}} \mathbf{M}^{-1} \hat{\mathbf{n}}}{(\hat{\mathbf{n}} \mathbf{M}^{-1} \mathbf{p})^2} \right)^{1/2} \right], \quad (23)$$

where \mathbf{p} and \mathbf{p}' are the momenta before and after the hop and M is the mass matrix. Because in the C + NO entrance channel the 2A and 4A states are degenerate and hopping between them due to numerical fluctuations and not because of the underlying physics, the hopping probability between the 2A and 4A states is calculated only after the sum of interatomic distances between all three interacting atoms is less than 12 a_0 (i.e., after the first entrance into the interaction region).

The electronic degeneracy factor for the TSH calculations is

$$g_e^{\text{TSH}}(T) = \frac{2 + 2\exp(-172.4/T) + 4\exp(-23.6/T)}{[1 + 3\exp(-23.6/T) + 5\exp(-62.4/T)][2 + 2\exp(-172.4/T)]}. \quad (24)$$

Here, $g_e^{\text{TSH}}(T)$ is obtained by adding Eq. (16) and a modified version of Eq. (15) which is valid when nonadiabatic transitions can occur.²¹

C. Time independent quantum mechanical method

To ascertain the accuracy of the QCT method, quantum mechanical (QM) probabilities have been calculated for $J = 0$ for the $\text{C}(^3\text{P}) + \text{NO}(X^2\Pi) \rightarrow \text{O}(^3\text{P}) + \text{CN}(X^2\Sigma^+)$, $\text{N}(^2\text{D})/\text{N}(^4\text{S}) + \text{CO}(X^1\Sigma^+)$ reaction at selected energies. Time independent quantum mechanical calculations are performed using the ABC code.⁴⁸ In this code, the time independent Schrödinger equation is solved in coupled-channel hyperspherical coordinates with a log-derivative propagator for a fixed value of J and corresponding triatomic parities (as defined in Ref. 48). Probabilities are obtained from the square of the scattering matrix elements.

Convergence of the TIQM calculations was monitored by systematically varying the two main convergence parameters (the maximum internal energy e_{max} and the maximum rotational quantum number of the diatom j_{max}) in each channel for a $J = 0$ calculation. These two parameters define the coupled-channel basis set for a single run. Initially, a number of test runs were carried out to converge the reaction probabilities with respect to these two parameters. The optimal values obtained for these parameters are $e_{\text{max}} = 3.0$ eV and $j_{\text{max}} = 90$ which includes a total of 4452 and 5742 ro-vibrational basis functions in the coupled-channel basis set for the ^2A and ^4A state, respectively. The number of log derivative propagation sectors (n_{sec}) and maximum hyperradius (ρ_{max}) was converged next. The optimal values of n_{sec} and ρ_{max} used for the TIQM calculations are 320 and 20 a_0 , respectively. With these four optimized parameters, the vibrational state resolved reaction probabilities could be converged to within 10^{-3} or better.

III. RESULTS AND DISCUSSION

A. The potential energy surfaces

In this work, the PESs for the [CNO] system for $^2\text{A}'$, $^2\text{A}''$, and $^4\text{A}''$ electronic states are constructed using the RKHS scheme from a large number of *ab initio* energies ($>15\,000$ for each PES). To test the quality of the PESs, additional 520 *ab initio* energies are calculated at off-grid points (R, r, θ) for the three different product channels for selected 1-dimensional cuts. A comparison between these reference MRCI+Q energies and the corresponding energies obtained from the RKHS interpolated PESs is shown in Fig. 2. As can be seen, for all the PESs, the *ab initio* energies are successfully reproduced by the RKHS interpolated analytical PESs. A good correlation ($R^2 = 0.9994$ to $R^2 = 0.9998$) between the *ab initio* and the RKHS interpolated energies for all three electronic states is found; see Fig. S1.

In the previously reported PESs,^{16,17,20} CASPT2 energies were fitted to a parameterized form including 255 linear and six non-linear parameters. The root mean square (RMS) deviation between reference values and the fit was 0.13 eV with a maximum deviation close to 1 eV, whereas in the relevant energy range for thermal collisions, the RMS was 0.094 eV.¹⁷ Hence, in addition to the higher level of theory (MRCI+Q) and the considerably better coverage of configurational space (~ 5000 vs. $\sim 50\,000$ points), the representation of the PESs from using a RKHS is also an improvement in the present work.

In Table III, the Morse parameters obtained from the diatomic potentials for the present PESs are tabulated along with the experimental results reported in Ref. 49. Good agreement is found for all the diatomic potentials. The r_{eqs} calculated from the analytical PESs are slightly (~ 0.02 a_0) longer than the experimental results. However, they are close to the distances obtained from *ab initio* calculations (2.2317, 2.1905,

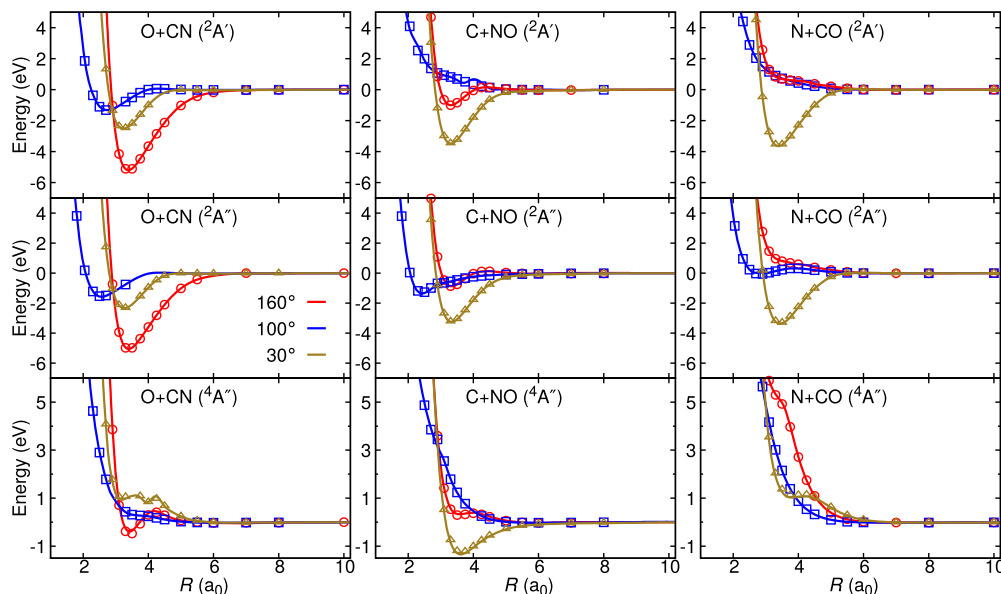


FIG. 2. Comparison between the *ab initio* energies (symbols) and the RKHS energies (solid lines) in Jacobi coordinates for the three reactant channels and for three different Jacobi angles. Jacobi coordinates are defined the same as shown in Fig. 1. The zero of energies is the reactant asymptotes of the corresponding channels. The *ab initio* energies are calculated at off-grid points and are not part of the RKHS interpolation grid.

TABLE III. Details of the Morse parameters for the diatoms computed from the analytical PESs. Experimental data obtained from the literature⁴⁹ are given in parentheses.

	D_e (eV)	r_{eq} (a_0)	ω_e (cm^{-1})	$\omega_e x_e$ (cm^{-1})
CN	7.3654	2.2336 (2.2144)	2031.347 (2068.705)	13.836 (13.144)
NO	6.1621	2.1923 (2.1747)	1864.690 (1903.68)	14.129 (13.97)
CO	10.8141	2.1502 (2.1318)	2131.903 (2170.21)	13.108 (13.461)

and 2.1505 a_0 , respectively, for CN, NO, and CO). The stationary configurations from the analytical surfaces and computed from electronic structure calculations are tabulated in Table IV. The $^2A'$ and $^2A''$ surfaces are degenerate for the collinear configurations, and the three stable minima correspond to different collinear arrangements of the atoms. A nonlinear minimum is also found for the $^2A''$ state along with the linear minima. Good agreement between the *ab initio* and analytical data (R within 0.01 \AA and E within 0.08 eV) was found, as shown in Table IV for the structures and energies of the minima.

Two-dimensional representations of the PESs are shown in Fig. 3. All PESs have a pronounced angular anisotropy. On the 2A PESs, the collinear and near collinear approaches for the C + NO collisions are favorable to form stable linear intermediates, whereas for the $^4A''$ state, the collinear approaches

TABLE IV. Energy and structures of few local minima of the analytical PESs for $^2A'$, $^2A''$, and $^4A''$ states of [CNO]. Bond lengths are given in atomic unit, and the energies are given in eV. Zero is set to the energy of $O(^3P) + C(^3P) + N(^4S)$. Values obtained from the *ab initio* energy calculations are given in parentheses. For the $^4A''$ state, one of the structures (C–NO) is a van der Waals complex with the NO separation (2.18 a_0) close to the equilibrium value (2.19 a_0). The PESs in Fig. 3 and the schematic in Fig. 1 also show the location of these minima.

	R_{CN}	R_{NO}	R_{CO}	Energy
Linear minima ($^2A'/^2A''$)				
C–N–O	2.2993 (2.2994)	2.3049 (2.3099)	4.6042 (4.6093)	−10.3811 (−10.3675)
N–C–O	2.3271 (2.3300)	4.5777 (4.5696)	2.2507 (2.2396)	−13.0570 (−13.0495)
C–O–N	4.7726 (4.7800)	2.5144 (2.5246)	2.2579 (2.2554)	−7.9001 (−7.8969)
Nonlinear minimum ($^2A''$)				
C–N–O	2.5430 (2.5416)	2.7414 (2.7304)	2.6338 (2.6223)	−9.7586 (−9.6777)
Nonlinear minimum ($^4A''$)				
C–N–O	2.6746	2.2756	4.4168	−7.7468
C–NO	5.4916	2.1849	4.0653	−6.2472
N–C–O	2.7742	4.3417	2.2446	−10.0788

for the C + NO collisions are repulsive and thus are not energetically favorable. Compared to the $^2A'$ surface, the topography of the $^2A''$ surface is a bit more complex. The nonlinear minimum and second order transition states can be seen in the

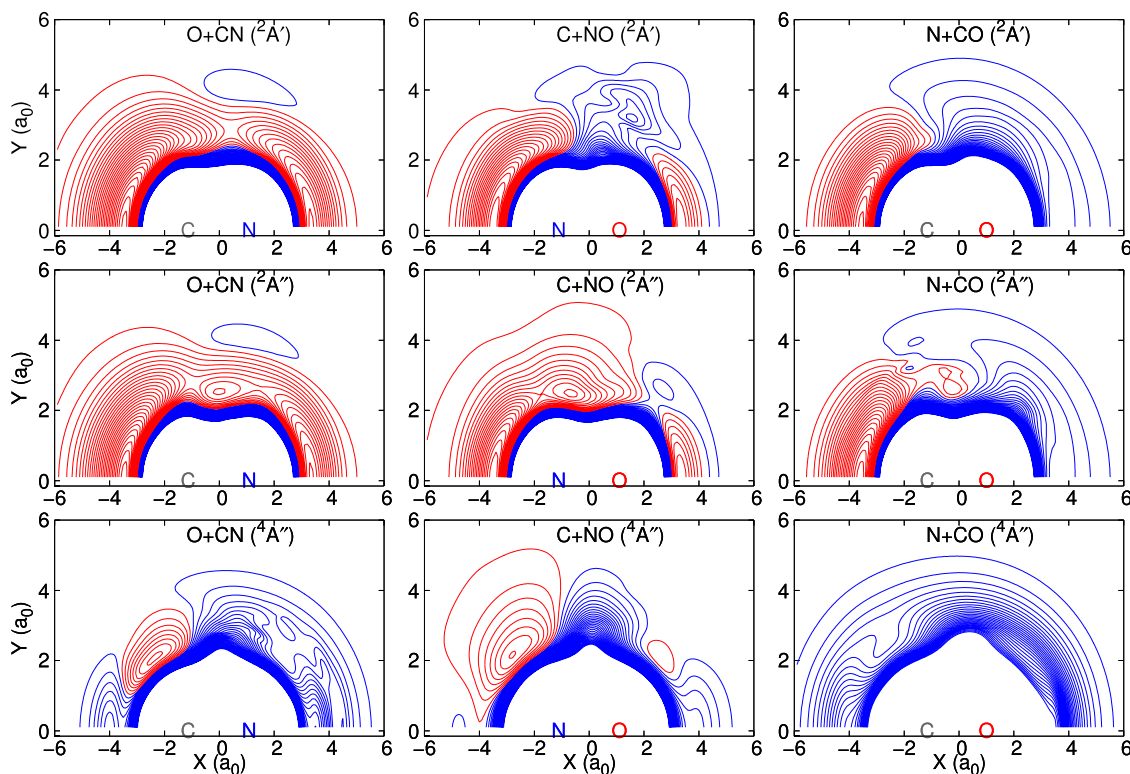


FIG. 3. Contour plots of the analytical PESs with the diatoms having bond distances fixed at their equilibrium distances. Spacing between the contour lines is 0.2 eV. The red lines correspond to negative energies (−0.1, −0.3, −0.5, . . . eV), and the blue lines correspond to positive energies (0.1, 0.3, 0.5, . . . eV). Zero of energies is set to the energy of the atoms and equilibrium configurations of the diatoms (i.e., 2.234, 2.192, and 2.150 a_0 , respectively, for CN, NO, and CO).

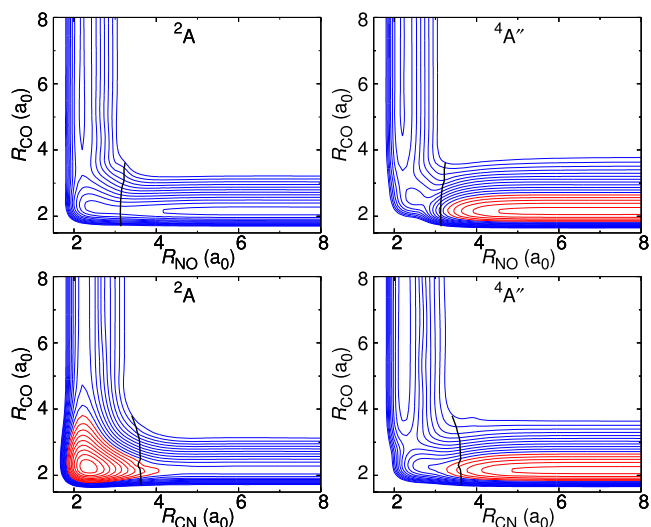


FIG. 4. Contour diagram of the analytical PESs for two different collinear arrangements: C–O–N is shown in the upper panel and N–C–O is shown in the lower panel. Both the $^2A'$ and $^2A''$ surfaces are degenerate for collinear configurations. Spacing between the contour lines is 0.5 eV. The blue lines represent the positive energies starting from 0.25 eV, while the red lines represent the negative energies starting from -0.25 eV. The zero of energy is set to the asymptotic energy of the $N(^4S) + CO(X^1\Sigma^+)$ channel. The black lines show the crossing seam between the doublet and quartet surface.

$^2A''$ and $^4A''$ surfaces which also exhibits two minima for nonlinear configurations which provides favorable attacking approaches for C + NO collisions. Conversely, near perpendicular approaches are favorable for C + NO collisions on the $^2A''$ PES due to the existence of a triangular minimum, whereas these paths are strongly repulsive on the $^2A'$ and $^4A''$

PESs. These different topologies mean that transitions between two such PESs will generate considerable torque.

Contour diagrams of the analytical PESs for collinear C–O–N and N–C–O geometries are shown in Fig. 4. The contour diagrams for the $^2A'$ states in Fig. 4 are analogous to those in Fig. 4 of Ref. 20. Minimum energy paths connecting different product channels of the PESs are reported in Fig. S2. The transition state found in the previous work²⁰ for C approaching to the NO from the O side can be seen in the present case (see upper panels in Figs. 4 and S2). The narrow passage due to the presence of a low barrier seen in the previous work²⁰ for the dissociation of NCO to N + CO can also be seen in Fig. S2. The crossing seam between doublet and quartet spin state PESs of the [CNO] system is shown in Fig. 4 with the black lines. The crossing occurs in the N + CO product channel.

B. Dynamical simulations

To validate using QCT simulations in the present work, first quantum mechanical (QM) calculations for the C + NO reaction for the $v = j = J = 0$ initial reactant state on all PESs were carried out for collision energies ranging from 0.05 to 0.8 eV. The QM results are then compared with their QCT counterparts in Figs. 5 and S3. It is found that QCT successfully reproduces the overall behavior of the QM total reaction probabilities in the investigated energy range. This is consistent with previous calculations for N + NO.³³ Depending on the PES, the distribution of the vibrational states changes significantly. Unlike the 2A PESs, for the $^4A''$ PES, only states up to $v' = 5$ for CO are present irrespective of the collision energy and lead to pronounced peaks at $v' = 2$ in the distributions (see Fig. 5,

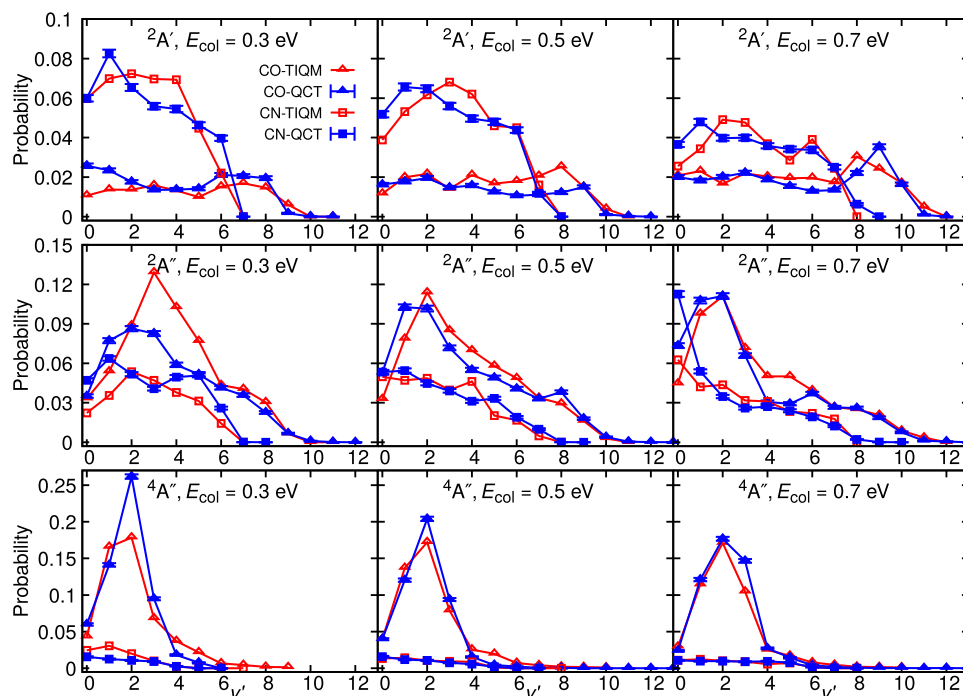


FIG. 5. Product vibrational state distributions (triangles and squares correspond to CO and CN product formation, respectively) at three different translational energies for the C + NO reaction and for the $v = j = J = 0$ initial reactant state obtained via TIQM (red symbols) and QCT (blue symbols, including statistical uncertainties) simulations performed on $^2A'$, $^2A''$, and $^4A''$ surfaces.

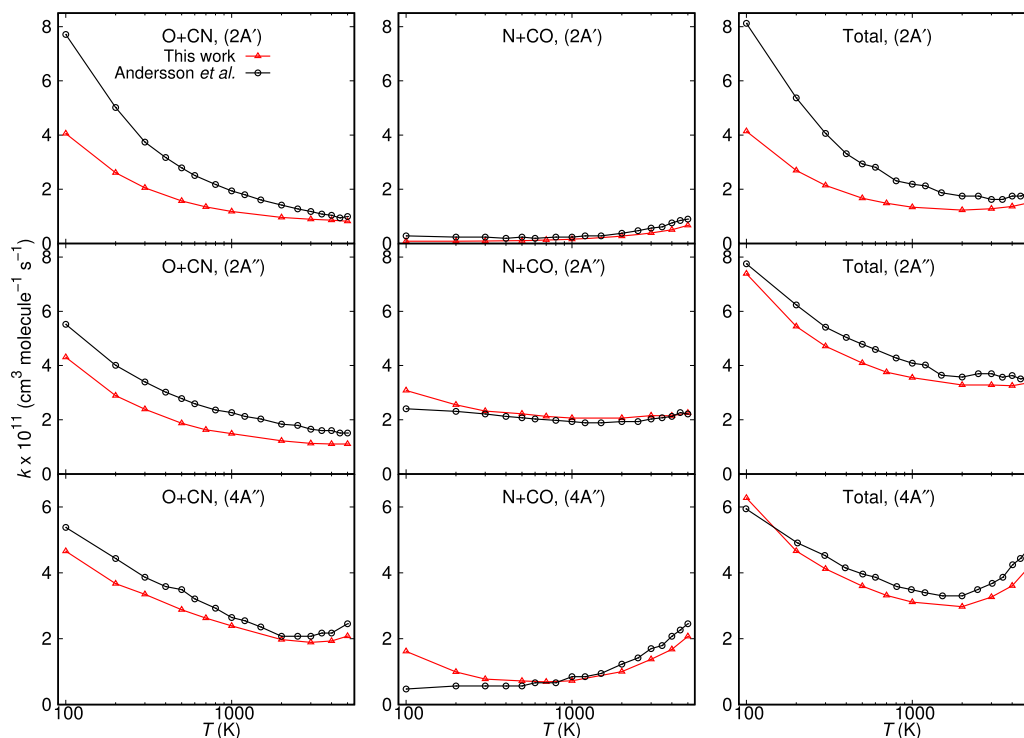


FIG. 6. Rate coefficients for the $C(^3P) + NO(X^2\Pi) \rightarrow O(^3P) + CN(X^2\Sigma^+)$, $N(^2D)/N(^4S) + CO(X^1\Sigma^+)$ over a range of temperatures from 100 to 5000 K. Theoretical and experimental results reported in the literature are also plotted.^{17,21,22} The rate coefficients from the previous theoretical work are divided by a factor of 2 to compare with the results obtained in this work (see text).

bottom row). It can also be seen that CN-formation is the most favorable for the dynamics on the $^2A'$ PES and comparatively less favorable on the $^4A''$ PES.

The differences in the vibrational state distributions on different PESs indicate that the dynamics of the C + NO reaction are strongly governed by the topology of the PESs. Irrespective of the PES and collision energy, QCT simulations yield distributions similar to the quantum simulations for all instances. Hence, QCT simulations are a meaningful way to efficiently investigate the reactive dynamics of the C + NO reaction.

The rate coefficients for the $C(^3P) + NO(X^2\Pi) \rightarrow O(^3P) + CN(X^2\Sigma^+)$, $N(^2D)/N(^4S) + CO(X^1\Sigma^+)$ reactions computed from adiabatic QCT simulations and carried out separately on the $^2A'$, $^2A''$, and $^4A''$ PESs are reported along with the available theoretical^{17,21,22} results in Fig. 6. The previous computed rate coefficients calculated on the 2A PESs are compared to the experimental results individually and thus multiplied by a factor of two because the 2A state exists in two different space symmetries. It can be seen in Fig. 6 that although the N + CO channel is more exothermic than the O + CN channel, the rate of N + CO formation is smaller than that for O + CN on the $^2A'$ surface. This can be explained by the presence of a barrier in the entrance channel of C + NO to form N + CO (see Fig. 3, right panel). However, for the $^2A''$ surface, another path is possible via the nonlinear minimum, which greatly enhances the rate for N + CO formation. The trajectories leading to O + CN do not involve a barrier in the entrance channel, and the rate for CN formation is large at low temperatures. These rates follow the typical behavior characteristic of barrierless

exothermic reactions. As seen in Fig. 6, the changing pattern of the rate coefficients as a function of temperature is similar to those reported in Refs. 20 and 22. The raw data of Fig. 6 are given in Table S1 of the [supplementary material](#).

The total rate coefficients for the title reaction are presented in Fig. 7 for temperatures between 15 and 4000 K and compared with the available experimental^{4,5,8-10} and theoretical¹⁷ results. The rates from adiabatic QCT simulations (red line) were carried out separately on the three PESs considered in this work. Very good agreement between computational

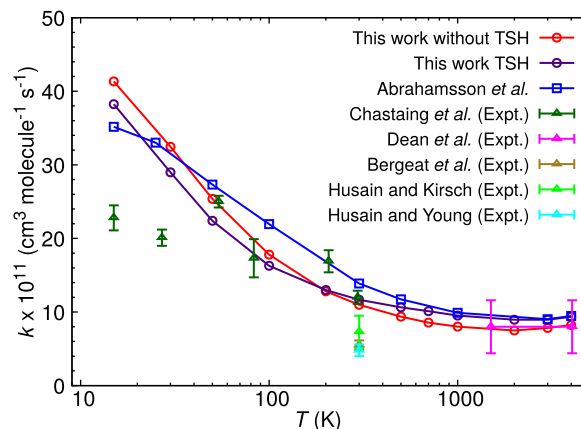


FIG. 7. Total rate coefficients for the $C(^3P) + NO(X^2\Pi) \rightarrow O(^3P) + CN(X^2\Sigma^+)$, $N(^2D)/N(^4S) + CO(X^1\Sigma^+)$ over a range of temperatures from 15 to 4000 K. Theoretical¹⁷ and experimental^{4,5,8-10} results reported in the literature are also plotted.

and the experimental results is found for $T > 50$ K in Fig. 7. As the temperature decreases, the computations deviate from the experimental results. A similar trend was also found in Ref. 17. This may be in part because the experiments for $T > 50$ K were carried out in Argon or N_2 as the buffer gas, whereas for temperatures below 30 K, helium was used. Conversely, it is possible that the calculations miss crossings to additional electronic states which may be relevant at low temperatures. At 50 K, $\sim 33\%$ of the molecules have less than 40 cm^{-1} of energy. Hence states and crossings to them which may be neglected in the present work would reduce the reaction rate at low temperature by $1/3$ without appreciably affecting the results at higher temperatures. The total rate calculated using TSH calculations following the Landau-Zener model is also presented in Fig. 7 (indigo line). Both the adiabatic and the TSH rate constants show a similar trend over the entire temperature range. However, the TSH rates overestimate the adiabatic results for high temperatures and underestimate it at low T . Below 50 K, both the adiabatic approach and the TSH approach cannot describe the low temperature rates for this reaction.

The branching ratio as a function of temperature (CN vs. CO production) is presented in Fig. 8(a) and compared with experimental values along with the theoretical results from Ref. 17. Two different experiments are available: one at 300 K and a second one for 2400–4000 K.^{8,9} They show that the branching fraction is almost T -independent although the error bar for the 300 K measurement is large. Although the branching fractions from simulations without nonadiabatic transitions computed in this work are larger than the theoretical work of Ref. 17, it underestimates the experimental value. Including nonadiabatic transitions leads to improved theoretical results which agree with the experimental branching fractions within statistical errors.^{8,9}

Considering the $C(^3P) + NO(X^2\Pi) \rightarrow N(^2D)/N(^4S) + CO(X^1\Sigma^+)$ channel, in particular, the predicted branching ratio for the generation of $N(^2D)$ vs. $N(^4S)$ as a function of T ranges between 60% and 80% for adiabatic simulations and

decreases to 50%, almost independent of temperature, when nonadiabatic effects are included; see Fig. 8(b). Since adiabatically the 2A states are only connected to $N(^2D)$ and the 4A state to $N(^4S)$, this branching ratio reflects the population statistics and the reaction barriers. With TSH included, population from the 2A state can transfer to the 4A PES increasing the amount of $N(^4S)$ created. This may provide a sensitive experimental probe of the importance of nonadiabatic effects in this reaction.

To explore the effect of including nonadiabatic transitions through surface hopping on the branching fraction for this reaction, the rate coefficients for CN and CO formation with and without TSH simulations are plotted in Fig. 8(c). Including TSH in the dynamics substantially increases CO formation, whereas it slightly reduces the probability for CN formation. This eventually leads to a branching fraction which is close to the experimental value.

For direct comparison with the vibrational distribution $P(v')$ of the CN from molecular beam experiments by Naulin *et al.*,¹¹ additional 4×10^5 trajectories on each of the surfaces are run at an average collision energy of 0.06 and 0.23 eV. The collision energies are sampled following Ref. 14 which was also used in Ref. 17. The initial velocities of C and NO are sampled from a Gaussian distribution

$$f(v) = v^2 \exp\left[-\frac{(v - v_s)^2}{\alpha_s^2}\right], \quad (25)$$

where v is the instantaneous velocity of the species in the molecular beam and v_s and α_s are the average speed and the width. For NO, these values are $v_s = 100\text{ ms}^{-1}$ and $\alpha_s = 818\text{ ms}^{-1}$ for both collision energies, whereas for the C atom, $v_s = 801$ and 2130 ms^{-1} and $\alpha_s = 84$ and 140 ms^{-1} are used for collision energies of 0.06 and 0.23 eV. The relative velocities between the two collision partners are then calculated considering that the beams are perpendicular to one another.

The results from runs on each of the PESs are combined by using weights according to Ref. 17: each of the 2A surfaces

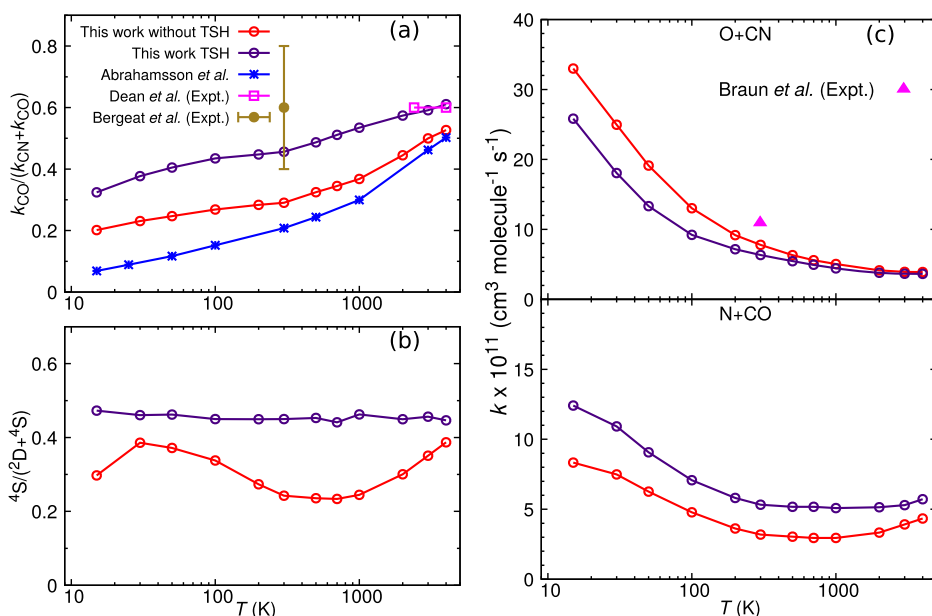


FIG. 8. Branching fractions of (a) CO and CN products, (b) 2D and 4S states of N in the N + CO channel, and (c) rate coefficients for the (top panel) $C(^3P) + NO(X^2\Pi) \rightarrow O(^3P) + CN(X^2\Sigma^+)$, (bottom panel) $N(^2D)/N(^4S) + CO(X^1\Sigma^+)$ reaction for $15 \leq T \leq 4000$ K, compared with available experimental^{3,8,9} and theoretical¹⁷ results. Red and indigo traces are from the present work without and with TSH.

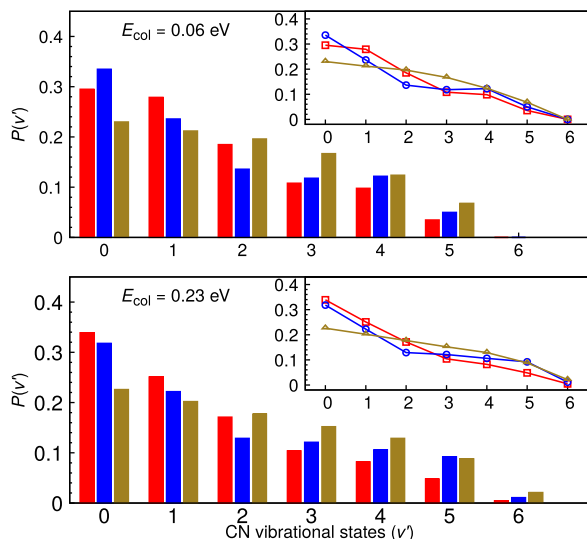


FIG. 9. Vibrational distribution of the products obtained from adiabatic dynamics (red) for the $C(^3P) + NO(X^2\Pi) \rightarrow O(^3P) + CN(X^2\Sigma^+)$ reaction at $E_{col} = 0.06$, and 0.23 eV of energy is compared with the crossed molecular beams experiments¹¹ (blue). Results reported in a QCT study¹⁷ by Abrahamsson *et al.* (olive) are also plotted. Insets show the line plots of the same.

contributes 0.25 and the $^4A''$ surface has a weight of 0.5. For the 2A states, 2 (one $J = 0$ and one $J = 1$ states) of the 18 fine structure states of the reactants remain active during reaction, while for the $^4A''$ state, 4 (the remaining two $J = 1$ states) of the 18 fine structure states of the reactants participate in the reaction. The vibrational distributions of the CN diatom are presented in Fig. 9 along with the experimental¹¹ results and the computations from Ref. 17. Compared to the results reported in Ref. 17, the present results agree well with the low v' state population and have a decay trend that matches the experimental results. The average energy distribution in the vibrational, rotational, and translational mode of the CN diatom is summarized in Table V. It is found that the present work underestimates the contribution from the vibrational mode. However, the fractional distributions agree well with the experiment.

The results obtained so far indicate that the present computations yield reliable results for rate coefficients, branching fractions, and final state distributions when compared with experiment except for low temperatures (<50 K). The range

TABLE V. Product energy distribution for the $C(^3P) + NO(X^2\Pi) \rightarrow O(^3P) + CN(X^2\Sigma^+)$ at two different collision energies. Quantities inside angle brackets are the average energies, $\langle \epsilon'_{vib} \rangle$, $\langle \epsilon'_{rot} \rangle$, and $\langle \epsilon'_{tra} \rangle$ for vibration, rotation, and translational motions, respectively, and f_i are the corresponding normalized fractions. The average energies are given in eV.

Energy		$\langle \epsilon'_{vib} \rangle$	f_{vib}	$\langle \epsilon'_{rot} \rangle$	f_{rot}	$\langle \epsilon'_{tra} \rangle$	f_{tra}
$E_{col} = 0.06$ eV	This work	0.37	0.30	0.19	0.15	0.69	0.55
	Expt. ¹¹	0.40	0.30	0.20	0.15	0.74	0.55
	Theor. ¹⁷	0.46	0.36	0.19	0.15	0.64	0.49
$E_{col} = 0.23$ eV	This work	0.37	0.26	0.26	0.18	0.80	0.56
	Expt. ¹¹	0.45	0.29	0.30	0.20	0.77	0.51
	Theor. ¹⁷	0.43	0.30	0.27	0.19	0.75	0.51

of temperatures covered by the experiments extends from 15 to 5000 K. However, the collisional and reactive dynamics of the [CNO] system are also relevant for hypersonic conditions for which temperatures can reach to 20 000 K. Hence, in the following, several important quantities for the $C(^3P) + NO(X^2\Pi) \rightarrow O(^3P) + CN(X^2\Sigma^+)$, $N(^2D)/N(^4S) + CO(X^1\Sigma^+)$ reactions in the hypersonic regime are determined from simulations at higher temperatures.

The rate coefficients for the C + NO reaction at temperatures between 5000 and 20 000 K are reported in Fig. 10. With increasing temperature, the rate constants increase. Including nonadiabatic transitions reduces the CN-formation probability and enhances CO production. It can be seen in Fig. 10 that both the TSH and adiabatic rate coefficients increase monotonically for both O + CN and N + CO production channels although the curvature changes for O + CN production rate below 12 000 K. At such high temperatures, a small fraction (0.2% and 2.6% at 10 000 and 20 000 K, respectively) of the trajectories also leads to full atomization, i.e., C + N + O. For practical calculations,⁵⁰ it is useful to fit the temperature-dependent rate to an Arrhenius expression; see Table VI.

Another key process for reactions in the hypersonic flow is the vibrational energy relaxation of the diatomic molecule as this is an effective channel for energy redistribution. This process is usually described by the vibrational relaxation time parameter $(p\tau_{vib})$ ^{34,51}

$$p\tau_{vib}(T) = \frac{k_B T}{k_{10}(T)(1 - e^{-\hbar\omega/k_B T})}, \quad (26)$$

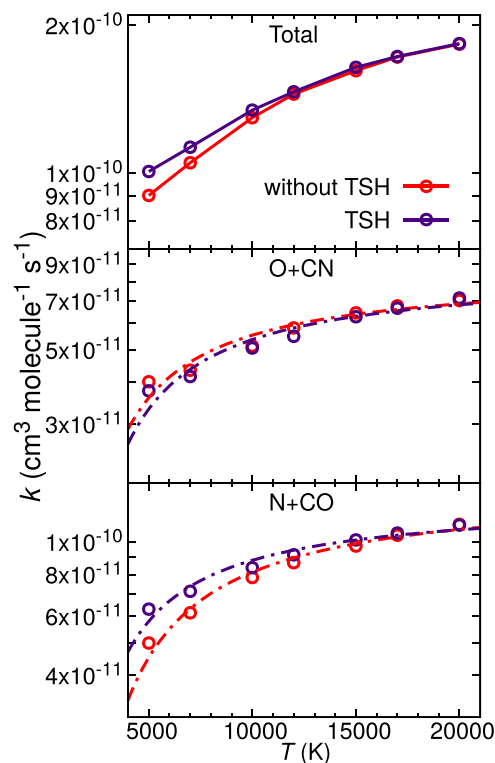


FIG. 10. Rate coefficients obtained from adiabatic and TSH simulations for the $C(^3P) + NO(X^2\Pi) \rightarrow O(^3P) + CN(X^2\Sigma^+)$, $N(^2D)/N(^4S) + CO(X^1\Sigma^+)$ reactions for temperatures 5000–20 000 K. Dashed-dotted lines correspond to the Arrhenius fit of the rates.

TABLE VI. Parameters obtained by fitting the rate constants (5000–20 000 K) for the $C(^3P) + NO(X^2\Pi) \rightarrow O(^3P) + CN(X^2\Sigma^+)$, $N(^2D)/N(^4S) + CO(X^1\Sigma^+)$ reactions to an Arrhenius expression. The rates obtained from these expressions have units in $\text{cm}^3 \text{ molecule}^{-1} \text{ s}^{-1}$ with $[A] = \text{cm}^3 \text{ molecule}^{-1} \text{ s}^{-1}$ and $[B] = \text{K}$.

Arrhenius expression: $k(T) = Ae^{-B/T}$			
Channel	Method	A	B
O + CN	Adiabatic	8.51×10^{-11}	4312
O + CN	TSH	8.66×10^{-11}	4782
N + CO	Adiabatic	1.46×10^{-10}	5876
N + CO	TSH	1.34×10^{-10}	4195

where p is the pressure and τ_{vib} is the vibrational relaxation time.^{51,52} Here, $k_{10}(T)$ is the rate coefficient for the vibrational transition from $v = 1$ to $v' = 0$ for inelastic collisions at temperature T , ω is the harmonic frequency of the diatom, and k_B is the Boltzmann constant.

To determine $p\tau_{\text{vib}}$ for the C + NO collision system, 40 000 trajectories were initiated on each of the three surfaces at temperatures between 1000 and 20 000 K, starting from $NO(v = 1, j')$. In these simulations, the rotational states j' of NO were sampled from a Boltzmann distribution and the relative translational energies were sampled following Eq. (17) for a particular temperature. The number of trajectories which relax to $NO(v' = 0, j')$, remain vibrationally excited $NO(v' > 0, j')$, form $CN(v', j')$, $CO(v', j')$, and decay to C + N + O are reported in Table S2. Vibrational relaxation to $NO(v' = 0, j')$ is more important at low temperatures and decreases to $\sim 1.4\%$ above 10 000 K, whereas vibrationally excited NO is the predominant final state for all temperatures. The formation of CN and CO accounts for up to 7% of the final products, whereas full atomization is a rare event.

Figure 11 (upper panel) reports $p\tau_{\text{vib}}(T)$ as a function of temperature. The value of $p\tau_{\text{vib}}(T)$ increases for higher temperature which indicates longer relaxation times. Considering the temperature dependence of the decay rate $k_{10}(T)$ and the Boltzmann factor in Eq. (26) separately reveals that the temperature dependence of $p\tau_{\text{vib}}(T)$ is primarily driven by the Boltzmann factor; see the middle and bottom panel of Fig. 11. The computed $p\tau_{\text{vib}}(T)$ can again be fit to an analytical expression

$$p\tau_{\text{vib}}(T) = 6.07 \times 10^{-5} e^{(-135.20/T^{1/3})} + 1.82 \times 10^{-11} T^{0.85} \quad (27)$$

for convenient use in reaction networks. This fit is also included in the top panel of Fig. 11. Because the overall behavior of $p\tau_{\text{vib}}(T)$ differs considerably from a non-reactive system such as Ar + CO,^{34,51} separate simulations were run for the N + CO collisions on $^4A''$ PES. The reason for considering this state is (a) its overall similarity of the PES with that for Ar + CO and (b) because reactive collisions are rare due to the presence of a barrier in the entrance channel (see Fig. 3). Simulations for a range of temperatures yield a very similar $k(T)$ as the one known from Ar + CO. Therefore, the behavior of $k(T)$ for C + NO as a function of T must be owed to the shape of the PES and the fact that reactive collisions are possible. It is worthwhile to note that for the $O_2 + O$ system, a similar T -dependence of $p\tau_{\text{vib}}(T)$ was found.^{53–55}

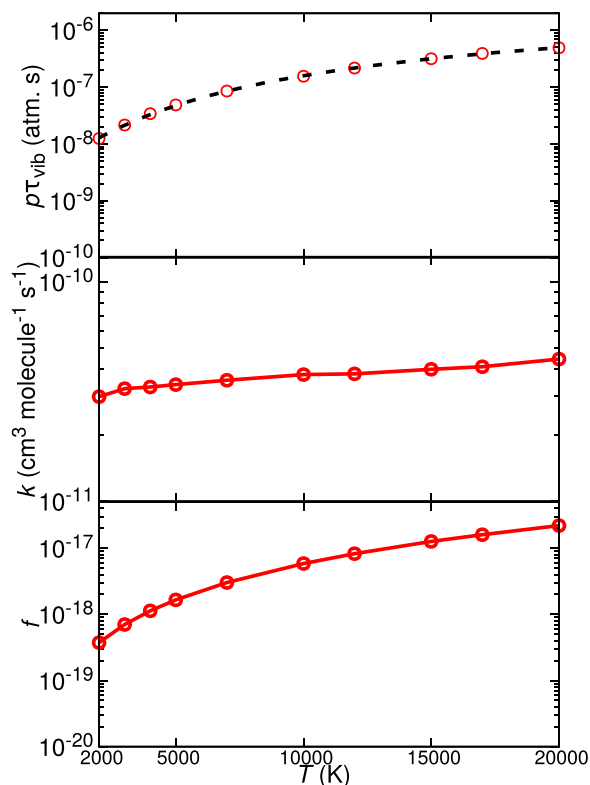


FIG. 11. Simulation results for the vibrational relaxation of C + NO collisions. Upper panel: $p\tau_{\text{vib}}(T)$ as a function of temperature. Black dashed line shows an analytical fit of the results (see text). Middle panel: $k_{10}(T)$ as a function of temperature. Lower panel: magnitude of the right-hand side of Eq. (26) excluding $k_{10}(T)$ from the denominator.

To investigate the differences in the behavior of $p\tau_{\text{vib}}(T)$ for C + NO compared with Ar + CO, the distribution of impact parameters for the reactive and vibrationally inelastic trajectories is reported in Fig. S4. Most of the trajectories with small impact parameters react to produce either CO or CN rather than changing the vibrational state of NO. In addition, the distributions of the lifetime (τ) for the deactivating collision complex for vibrationally relaxed trajectories are presented in Fig. 12. The lifetime of the collision complex is defined as the time elapsed between satisfying a geometrical criterion (the sum of the three inter-atomic distances is smaller than the cutoff value of $12 a_0$) for the first time until the time when it is not fulfilled anymore. As can be seen in Fig. 12, the complex lifetimes are all short—shorter than 1 ps. Next, the maximum of $p(\tau)$ shifts to shorter times with increasing temperature. And finally, the cumulative probability is steep and reaches almost 100% for $T = 20\,000$ K by $\tau = 250$ fs, whereas it flattens out for lower temperatures.

Taken together, the present simulations suggest that the vibrational relaxation times as a function of temperature are influenced by two factors. First, the fact is that “parasitic processes” such as reactive rearrangements can take place which affect the probability for vibrational relaxation. Second, the short lifetime of the collision complex independent of temperature and the increase of the rate by over 4 orders of magnitude compared to simpler rare-gas collisions at low temperatures leads to an almost T -independent rate $k_{10}(T)$ of the vibrational relaxation. This also means that the vibrational coordinates are not broadly sampled, one of the requirements for vibrational

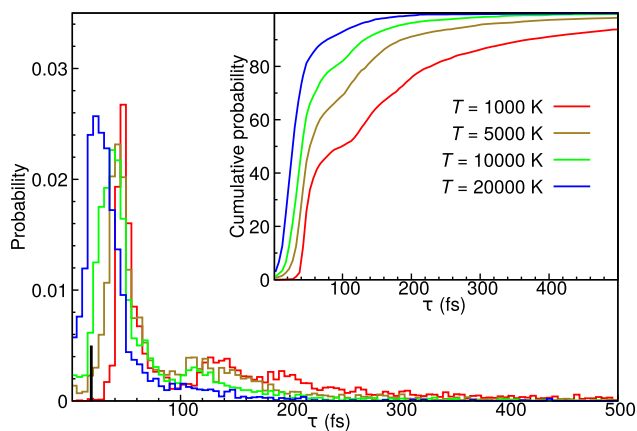


FIG. 12. Distribution of the lifetimes (τ) for the collision complex for the trajectories lead to vibrational relaxation to $\text{NO}(v' = 0, j')$ at different temperatures. The black line at ~ 18.3 fs represents the vibrational time period of $\text{NO}(v = 1, j = 0)$. Inset: the cumulative distribution function of τ in percentage.

relaxation. Both these effects must be responsible for the rather unusual shape of $p\tau_{\text{vib}}(T)$.

IV. CONCLUSION

The present work provides a comprehensive characterization of the $\text{C}(^3\text{P}) + \text{NO}(X^2\Pi) \rightarrow \text{O}(^3\text{P}) + \text{CN}(X^2\Sigma^+)$, $\text{N}(^2\text{D})/\text{N}(^4\text{S}) + \text{CO}(X^1\Sigma^+)$ reactions using fully dimensional PESs represented as a RKHS for the $^2A'$, $^2A''$, and $^4A''$ states. The use of quasiclassical trajectory simulations is justified by direct comparison with results from quantum mechanical simulations. For the experimentally characterized temperature range, favorable agreement between computations and experiments is found for the rate coefficients, branching fractions, and final state distributions. Compared to adiabatic simulation, the inclusion of nonadiabatic transitions between different electronic states for the title reaction leads to a better agreement with the experimental branching fraction. For temperatures relevant to the hypersonic flight regime, the rate coefficients and vibrational relaxation times were determined and empirical expressions are provided which can be used in reaction network modeling.

SUPPLEMENTARY MATERIAL

See [supplementary material](#) for Figures S1, S2, S3, and S4 and Tables S1 and S2.

ACKNOWLEDGMENTS

Part of this work was supported by the United State Department of the Air Force which is gratefully acknowledged (to M.M.). Support by the Swiss National Science Foundation through Grant No. 200021-117810, the NCCR MUST (to M.M.), and the University of Basel are also acknowledged.

¹N. Lamoureux, H. E. Merhubi, L. Pillier, S. de Persis, and P. Desgroux, *Combust. Flame* **163**, 557 (2016).

²G. I. Boger and A. Sternberg, *Astrophys. J.* **632**, 302 (2005).

³W. Braun, A. M. Bass, D. D. Davis, and J. D. Simmons, *Proc. R. Soc. A* **312**, 417 (1969).

⁴D. Husain and L. J. Kirsch, *Chem. Phys. Lett.* **8**, 543 (1971).

⁵D. Husain and A. N. Young, *J. Chem. Soc., Faraday Trans. 2* **71**, 525 (1975).

⁶K. J. Schmatjko and J. Wolfrum, *Ber. Bunsenges. Phys. Chem.* **82**, 419 (1978).

⁷P. Halvick, J. C. Rayez, and E. M. Evleth, *J. Chem. Phys.* **81**, 728 (1984).

⁸A. J. Dean, R. K. Hanson, and C. T. Bowman, *J. Phys. Chem.* **95**, 3180 (1991).

⁹A. Bergeat, T. Calvo, G. Dorthe, and J. C. Loison, *Chem. Phys. Lett.* **308**, 7 (1999).

¹⁰D. Chastaing, S. D. Le Picard, and I. R. Sims, *J. Chem. Phys.* **112**, 8466 (2000).

¹¹C. Naulin, M. Costes, and G. Dorthe, *Chem. Phys.* **153**, 519 (1991).

¹²M. Costes, C. Naulin, N. Ghanem, and G. Dorthe, *J. Chem. Soc., Faraday Trans.* **89**, 1501 (1993).

¹³P. Halvick and J. C. Rayez, *Chem. Phys.* **131**, 375 (1989).

¹⁴E. Wallin, P.-A. Elofson, and L. Holmild, *Chem. Phys.* **163**, 37 (1992).

¹⁵M. Simonson, N. Marković, S. Nordholm, and B. J. Persson, *Chem. Phys.* **200**, 141 (1995).

¹⁶S. Andersson, N. Marković, and G. Nyman, *Chem. Phys.* **259**, 99 (2000).

¹⁷E. Abrahamsson, S. Andersson, N. Marković, and G. Nyman, *Phys. Chem. Chem. Phys.* **10**, 4400 (2008).

¹⁸B. J. Persson, B. O. Rots, and M. Simonson, *Chem. Phys. Lett.* **234**, 382 (1995).

¹⁹O. Yazidi, H. Gritli, and G. Chambaud, *Mol. Phys.* **103**, 3321 (2005).

²⁰S. Andersson, N. Marković, and G. Nyman, *Phys. Chem. Chem. Phys.* **2**, 613 (2000).

²¹S. Andersson, N. Marković, and G. Nyman, *J. Phys. Chem. A* **107**, 5439 (2003).

²²T. J. Frankcombe and S. Andersson, *J. Phys. Chem. A* **116**, 4705 (2012).

²³C. E. M. Gonçalves, B. R. L. Galvão, V. C. Mota, J. P. Braga, and A. J. C. Varandas, *J. Phys. Chem. A* **122**, 4198 (2018).

²⁴I. Armenise and F. Esposito, *Chem. Phys.* **446**, 30 (2015).

²⁵H.-J. Werner, P. J. Knowles, G. Knizia, F. R. Manby, and M. Schütz, *Wiley Interdiscip. Rev.: Comput. Mol. Sci.* **2**, 242 (2012).

²⁶T. H. Dunning, Jr., *J. Chem. Phys.* **90**, 1007 (1989).

²⁷D. E. Woon and T. H. Dunning, Jr., *J. Chem. Phys.* **98**, 1358 (1993).

²⁸D. E. Woon and T. H. Dunning, Jr., *J. Chem. Phys.* **100**, 2975 (1994).

²⁹T.-S. Ho and H. Rabitz, *J. Chem. Phys.* **104**, 2584 (1996).

³⁰O. T. Unke and M. Meuwly, *J. Chem. Inf. Model.* **57**, 1923 (2017).

³¹J. C. Castro-Palacio, T. Nagy, R. J. Bemish, and M. Meuwly, *J. Chem. Phys.* **141**, 164319 (2014).

³²O. T. Unke, J. C. Castro-Palacio, R. J. Bemish, and M. Meuwly, *J. Chem. Phys.* **144**, 224307 (2016).

³³O. Denis-Alpizar, R. J. Bemish, and M. Meuwly, *Phys. Chem. Chem. Phys.* **19**, 2392 (2017).

³⁴O. Denis-Alpizar, R. J. Bemish, and M. Meuwly, *J. Chem. Phys.* **146**, 111102 (2017).

³⁵D. G. Truhlar and J. T. Muckerman, in *Atom—Molecule Collision Theory*, edited by R. B. Bernstein (Springer US, 1979), pp. 505–566.

³⁶N. E. Henriksen and F. Y. Hansen, *Theories of Molecular Reaction Dynamics* (Oxford, 2011).

³⁷L. Bonnet and J.-C. Rayez, *Chem. Phys. Lett.* **277**, 183 (1997).

³⁸L. Bonnet and J.-C. Rayez, *Chem. Phys. Lett.* **397**, 106 (2004).

³⁹J. D. Bender, P. Valentini, I. Nompelis, Y. Paukku, Z. Varga, D. G. Truhlar, T. Schwartzentruber, and G. V. Candler, *J. Chem. Phys.* **143**, 054304 (2015).

⁴⁰J. R. Stine and J. T. Muckerman, *J. Chem. Phys.* **65**, 3975 (1976).

⁴¹L. D. Landau, *Phys. Z. Sowjet.* **2**, 46 (1932).

⁴²C. Zener, *Proc. R. Soc. A* **137**, 696 (1932).

⁴³A. K. Belyaev and O. V. Lebedev, *Phys. Rev. A* **84**, 014701 (2011).

⁴⁴A. K. Belyaev, C. Lasser, and G. Trigila, *J. Chem. Phys.* **140**, 224108 (2014).

⁴⁵A. K. Belyaev, W. Domcke, C. Lasser, and G. Trigila, *J. Chem. Phys.* **142**, 104307 (2015).

⁴⁶W. Xie and W. Domcke, *J. Chem. Phys.* **147**, 184114 (2017).

⁴⁷W. H. Miller and T. F. George, *J. Chem. Phys.* **56**, 5637 (1972).

⁴⁸D. Skouteris, J. F. Castillo, and D. E. Manolopoulos, *Comput. Phys. Commun.* **133**, 128 (2000).

⁴⁹K. P. Huber and G. Herzberg, *Molecular Spectra and Molecular Structure. IV. Constants of Diatomic Molecules* (Van Nostrand, New York, 1979).

⁵⁰G. A. Bird, *Molecular Gas Dynamics and the Direct Simulation of Gas Flows* (Clarendon Press, 1994).

⁵¹R. C. Millikan and D. R. White, *J. Chem. Phys.* **39**, 3209 (1963).

⁵²E. E. Nikitin and J. Troe, *Phys. Chem. Chem. Phys.* **10**, 1483 (2008).

⁵³J. E. Breen, R. B. Quyy, and G. P. Glass, *J. Chem. Phys.* **59**, 556 (1973).

⁵⁴K. Kalogerakis, R. Copeland, and T. Slinger, *J. Chem. Phys.* **123**, 194303 (2005).

⁵⁵D. A. Andrienko and I. D. Boyd, *J. Thermophys. Heat Transfer* **0**, 1 (2016).